Simultaneous 3D Imaging of Bone and Vessel Microstructure in a Rat Model

Max Langer, Rhonda Prisby, Zsolt Peter, Alain Guignandon, Marie-Hélène Lafage-Proust, and Françoise Peyrin

***Abstract*—Analysis of bone microvascularization has generally been performed from 2D histology. The method proposed in this study enables for the first time to simultaneously analyze, in 3D, the microvascularization and bone microstructure in a rat model. The method is based on the use of quantitative synchrotron micro-computed tomography (SR-μCT) coupled to an automatic image analysis procedure. It was applied to investigate the effect of intermittent parathyroid hormone (PTH) administration on angiogenesis and osteogenesis in rats. Rats were posthumously injected with a contrast agent and subsequently imaged. The algorithm allowed the reconstruction and the segmentation of both bone microstructure and microvascularization in cortical and trabecular regions. A large set of 3D quantitative parameters were then extracted from the bone and vascular networks. In particular, we propose a new parameter, utilizing the availability of both microstructures to relate the two, which we dub the vascular-trabecular interdistance (VTI). Due to the short acquisition times of SR-μCT and the efficiency of the image analysis algorithm, a large data set was analyzed, which permitted statistical analysis of the measured parameters. Statistical analysis confirmed that treatment with PTH significantly modulated several bone and vessel parameters, including the VTI.**

***Index Terms*—Biomedical imaging, blood vessels, bones, synchrotron radiation, X-ray tomography.**

I. Introduction

BONE vascularization plays a major role in many physiological events such as fracture healing and bone growth, and pathological processes such as metastasis, Paget's disease and hematopoïetic disorders [1]. Moreover, bone blood supply has been recently shown to be involved in osteoporosis, the most frequent metabolic bone disease [2]. Further, the effects of anti-osteoporotic treatment on bone vascularization have yet to be investigated. The anatomical characterization of the bone vascular network was performed many years ago using 2D X-Ray imaging after intravascular opacification with contrast products in animal models [3]. Other data were provided by histological analyses of vessels in bone [4]. Bone microstructure has been extensively investigated using microcomputed tomography (μCT) [5]–[13]. However, these methods have not permitted precise quantification and imaging of the vascular network in three dimensions (3D). μCT has previously been applied to imaging of the vascular microstructure [14], [15]. However, these studies were carried out on decalcified bone. Therefore they did not permit a full analysis of the spatial relationships between bone and vascular system. The mentioned studies focused on analyzing either bone microstructure or microvascularization separately.

The purpose of this work was to develop a new method in order to quantify simultaneously the 3D organization of bone microstructure and microvascularization in a rat model. We used synchrotron radiation 3D microcomputed tomography (SR-μCT) at the European Synchrotron Radiation Facility (ESRF), Grenoble, France [12]. The high flux of third generation synchrotron sources permits monochromatization of the X-ray beam, which yields a quantitative CT reconstruction of the energy dependent linear attenuation coefficient, and allows reaching micrometric spatial resolution with maintained efficiency [13]. Imaging was performed on rat samples posthumously injected with a contrast agent at a high spatial resolution (voxel size $2.8\ \mu\mathrm{m}^3$) to correctly resolve the microvasculature.

An automatic image analysis method was developed to identify cortical and trabecular bone envelopes, and then bone and vascular structure within each envelope. Characteristic 3D quantitative parameters were then extracted from both microstructures. In addition, since we have access to both bone and vascular microstructures simultaneously, it is interesting to quantify their spatial relationship. We did this by introducing a new parameter, which we dubbed the vascular-trabecular interdistance (VTI), which we defined as the average local distance between vessels lying in the trabecular bone region to the trabeculae. The method was applied to investigate the effect of the potentially anti-osteoporotic agent parathyroid hormone (PTH) on the bone and vascular networks in rats.

II. Materials and Methods

A. Sample Preparation

Rats were given either PTH (sc, $100\ \mu\mathrm{g/kg/day}$) for 5 days per week for 4 weeks or placebo (0.9% saline). Following euth-

M. Langer is with Creatis, CNRS UMR 5220, INSERM U630, Université de Lyon, INSA Lyon, F-69621 Villeurbanne Cedex, France, the European Synchrotron Radiation Facility, F-38043 Grenoble, France, and also with the Julius Wolff Institute & Berlin-Brandenburg School for Regenerative Therapies, Charité-Universitätsmedizin Berlin, 13353 Berlin, Germany (e-mail: max.langer@esrf.fr).

R. Prisby is with LBTO, INSERM U890, Université de Lyon, F-42023 St-Etienne, France and also with the Department of Kinesiology, University of Texas at Arlington, Arlington, TX 76019 USA(e-mail: prisby@uta.edu).

Z. Peter was with Creatis, CNRS UMR 5220, INSERM U630, Université de Lyon, INSA Lyon, F-69621 Villeurbanne Cedex, France. He is now with the GTE Department, University of Paris 10, PST/IUT of Ville d'Avray, F-92410 Ville d'Avray, France (e-mail: peterzs13@yahoo.com).

A. Guignandon and M. H. Lafage-Proust are with LBTO, INSERM U890, Université de Lyon, F-42023 St-Etienne, France (e-mail: alain.guignandon@univ-st-etienne.fr; mh.lafage.proust@univ-st-etienne.fr).

F. Peyrin is with Creatis, CNRS UMR 5220, INSERM U630, Université de Lyon, INSA Lyon, F-69621 Villeurbanne Cedex, France and also with the European Synchrotron Radiation Facility, F-38043 Grenoble, France (e-mail: peyrin@esrf.fr).

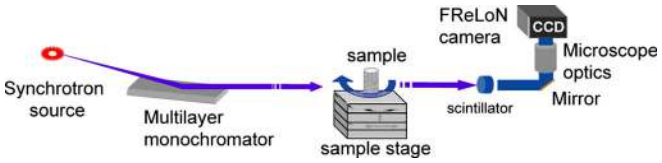

Fig. 1. Schematic of the imaging setup [12]. Monochromatic X-rays at 25 keV were selected from undulator radiation with a single reflection multilayer monochromator. Samples were mounted on a sample stage (3D translations and rotation) for tomographic imaging. A FreLoN [16] camera was used for detection.

anization, the rats were subsequently infused with a barium sulfate solution (contrast agent). The femora were dissected, fixed in 10% paraformaldehyde for 3 days, then transferred to and stored in 100% acetone, and subsequently embedded in methylmethacrylate (MMA). Of these embedded femora, small subsamples (parallelepiped side ~ 4 mm) were cut for imaging. In total 18 femur samples were prepared, 9 from controls and 9 from PTH treated rats.

B. Image Acquisition

3D SR-μCT imaging was performed on beamline ID19 at the ESRF, where a parallel beam 3D μCT setup has been developed [12] (Fig. 1). It consisted in recording 2000 radiographs of the sample under different angles of view over 360° using a FreLoN camera: a 2048 × 2048 pixel CCD-based detector [16]. The imaging system was set up to give a pixel size of 2.8 μm on the detector, yielding a cylindrical field of view (FOV) of diameter 5.6 mm. The energy was set to 25 keV, selected from undulator radiation using a single reflection multilayer monochromator, giving a beam height of approximately 2 mm (700 pixels). Exposure time was set to 0.25 s per image to ensure a large dynamic range (the detector provides 14 bits). The acquisition time for one scan was about 18 minutes.

For each sample, two images corresponding respectively to a region of interest in the metaphysis (ROI1) and diaphysis (ROI2) were acquired. Projections are shown in Fig. 2 and tomographic slices in Fig. 3. The ROI1 which was anatomically larger at the top did not completely fit the FOV. To avoid truncated projections, it was scanned in a non-conventional acquisition procedure, recording images over 360° with the axis of rotation displaced to the edge of the FOV. In this case after merging the projections separated by 180°, it was possible to reconstruct a larger FOV which encompassed the whole sample (note that the apparent truncation in Fig. 3 is physical, due to some samples being damaged in the sample preparation procedure, not due to truncated projections). This procedure yielded reconstructed 3D images of $2500 \times 2500 \times 700$ voxels.

C. Image Segmentation

The segmentation step required identifying vessels, bone and background. In addition, since it was desired to separately analyze trabecular and cortical bone, trabecular and cortical bone envelopes had to be identified.

There were specific problems in this study that needed to be addressed. Separating the trabecular and cortical bone compartments automatically was not straightforward, since there was

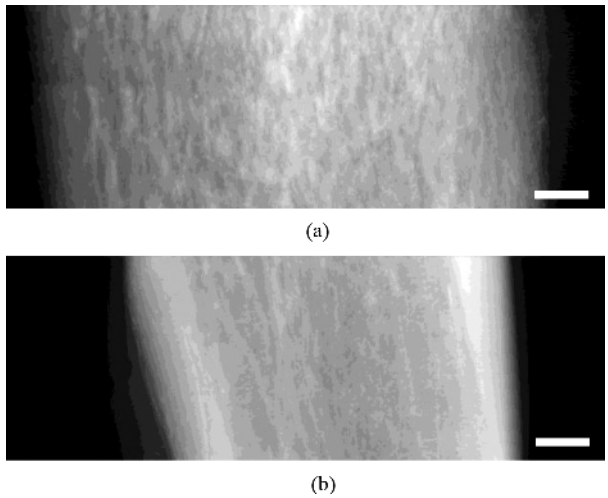

Fig. 2. Projections in the (a) Metaphysis (ROI1) and (b) Diaphysis (ROI2). Scale bar shows 0.5 mm.

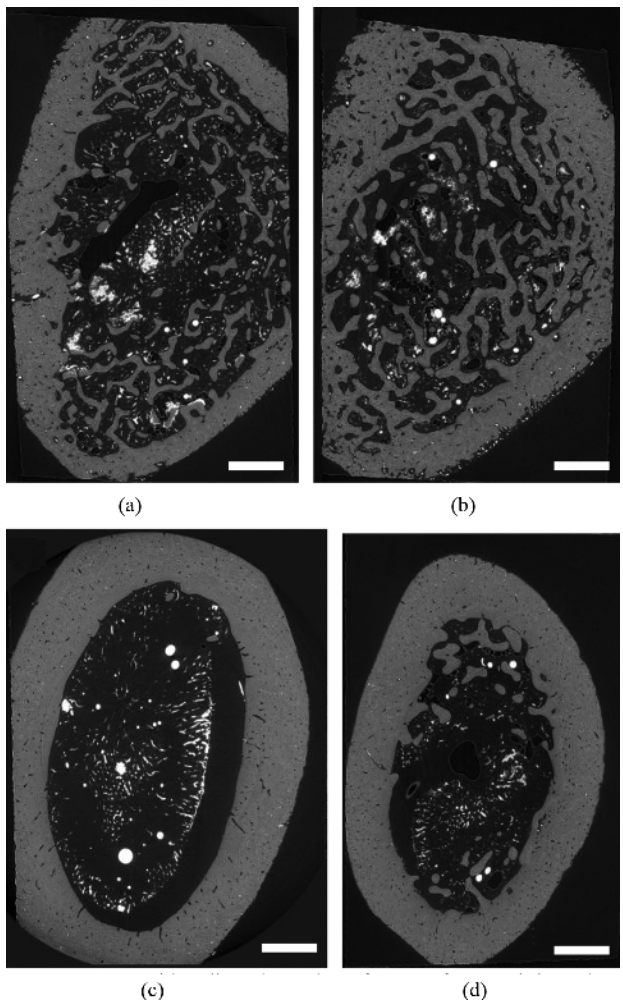

Fig. 3. Tomographic slice through a femur of a rat injected with contrast agent and embedded in methylmethacrylate (MMA) (a) Control sample, ROI1 (b) PTH sample, ROI2 (c) Control sample, ROI2 (d) PTH sample, ROI2. All phases are visible on the slice: vessels brightest (due to the contrast agent), bone as light gray, MMA as dark gray and air as black. The scale bar corresponds to 1 mm.

no measurable difference in grayscale between the two types of bone (Fig. 4). The high spatial resolution (2.8 μm) enabled imaging of the vascularization, but also allowed to resolve pores

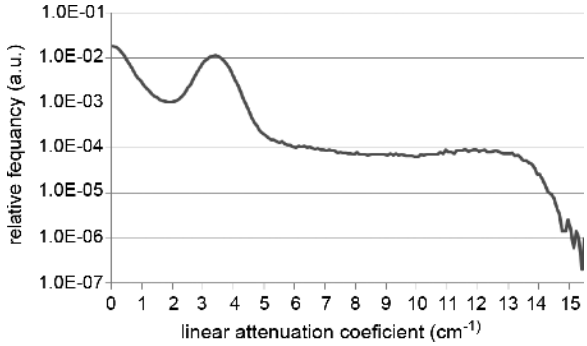

Fig. 4. Grayscale histogram of one sample. Bone has one distinct peak at 3.34. Contrast agent has a very wide peak at 13.31, which extends into lower values mainly due to partial volume effect.

(lacunae) in both cortical and trabecular bone. The recorded volumes were very large due to the large detector size. This puts stringent requirements on time and memory complexity of the image processing algorithm.

Bone and vessels were segmented by thresholding, with the threshold on the linear attenuation coefficient dividing bone and background set to 1.94. The threshold was determined with Otsu's method [17]. Vessels were then segmented using hysteresis thresholding to overcome partial volume effect, with a high threshold at 5.86 (selected with Otsu's method) and a low threshold at 5.66. The vessels were then subtracted from the first segmentation to separate the bone and vessel compartments. The two compartments were subsequently smoothed and denoised by one closing operation.

In ROI2, it was observed that the cortical bone generally has a thicker cross-section. To use this information, the 3D local thickness map, providing at each point of the volume the diameter of the largest sphere that fits inside the compartment of the point under consideration, as introduced in previous works [18], [19], was computed in the bone compartment. Since this measurement has to be done at the macroscopic scale, the porosities within the bone were first filled, effectively yielding the bone envelope. Segmentation of cortical bone could be performed by thresholding the 3D local thickness map. This yielded the envelope of the cortical bone. This volume was then used to separate bone into trabecular and cortical bone, and vessels into cortical and internal vessels by arithmetical operations. The total volume was calculated by filling in pores in the bone volume with a median filter, then filling in the empty space spanned by the bone.

After segmentation, each volume was partitioned into seven subvolumes (Fig. 5): Cortical volume, Trabecular volume, Pore volume in cortical bone, Pore volume in trabecular bone, Vessel volume in cortical volume, Vessel volume in Inner volume, Marrow Volume. 3D renderings of bone and vessel volumes are shown in Fig. 6. An apparent increase of vessel and trabecular thickness in the PTH sample is noticeable.

D. Extraction of Quantitative Parameters

From this splitting, it was possible to recover all other desired subvolumes. For instance the cortical bone envelope is the union of the cortical volume, pore volume in cortical bone and vessel volume in cortical volume.

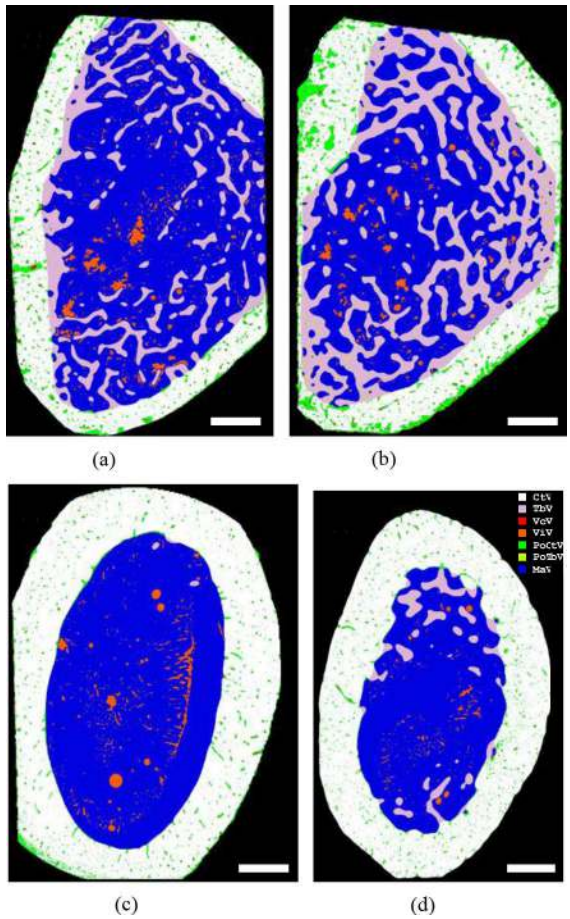

Fig. 5. Labeled volume consisting of the different segmented volumes (a) Control sample, ROI1 (b) PTH sample, ROI2 (c) Control sample, ROI2 (d) PTH sample, ROI2. All desired bone parameters can be calculated based on this volume. Scale bars indicate 1 mm.

Several parameters were extracted from the segmented volumes. The volume of each compartment was directly measured by counting voxels. The measured volumes were

- Total volume (TV): volume spanned by the outer contour of the cortical bone
- Inner volume (IV): volume spanned by the inner contour of the cortical bone
- Bone volume (BV)
- Cortical volume (Ct.V)
- Cortical envelope volume (Ct.TV): volume of cortical bone with porosity filled in
- Trabecular volume (Tb.V)
- Trabecular envelope volume (Tb.TV): volume of trabecular bone with porosity filled in
- Total vessel volume (VV)
- Vessel volume inside cortical envelope (VcV)
- Vessel volume inside inner volume (ViV)
- Marrow volume (Ma.V)
- Volume of pores in cortical bone (Ct.Po.V)
- Volume of pores in trabecular bone (Tb.Po.V)

To allow for comparison between samples, normalized ratios were calculated:

- Bone ratios: BV/TV, Ct.V/TV, Ct.TV/TV, Tb.V/IV, Tb.TV/IV

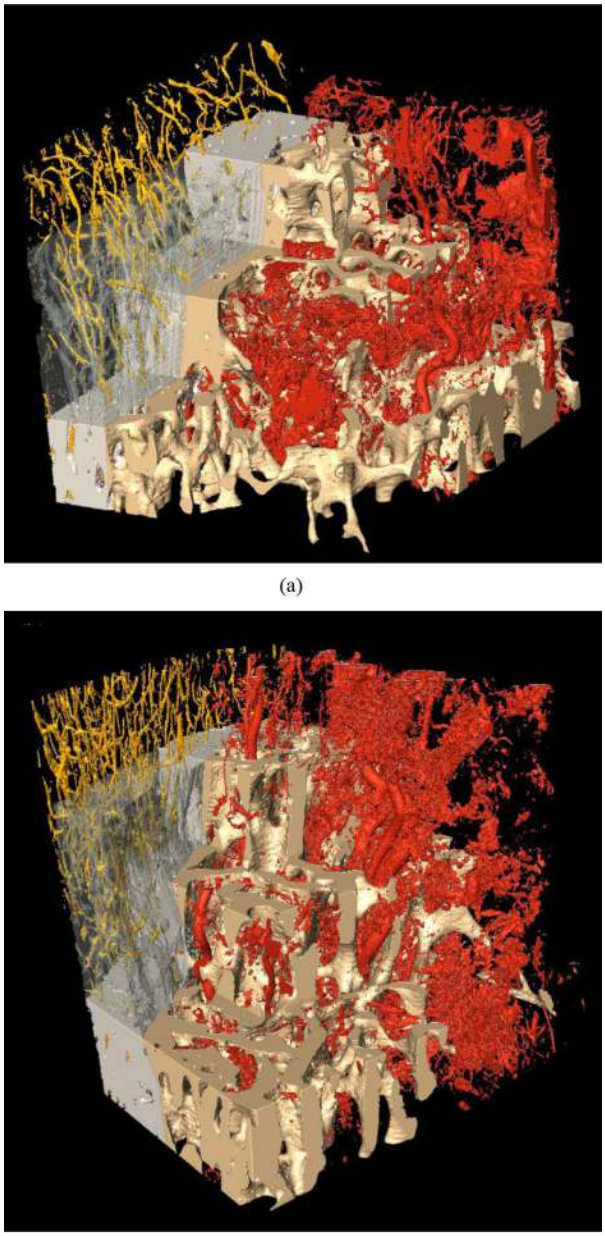

Fig. 6. Volume rendering showing bone and vessel compartments in ROI1. Cortical bone is in gray, trabecular bone in beige, vessel within trabecular bone in red and within cortical bone in orange (a) Control sample (b) PTH sample.

- Vessel ratios: VV/TV, VcV/Ct.V, ViV/IV, ViV/Ma.V
- Porosity ratios: Ct.Po (as Ct.Po.V/Ct.TV), Tb.Po (Tb.Po.V/Tb.TV)
- Marrow ratio: Ma.V/TV

Based on the segmented volumes, more complex parameters have also been extracted. Local thickness of bone and vessel compartments were calculated, yielding

- Mean cortical thickness (Ct.Th)
- Mean trabecular thickness (Tb.Th)
- Mean vessel thickness (V.Th)
- Mean thickness of internal vessels (Vi.Th)
- Mean thickness of cortical vessels (Vc.Th)

Since the SR-μCT is quantitative with respect to the linear attenuation coefficient, it was possible to evaluate the degree of mineralization of bone (DMB) [13]. To quantify the DMB within the different compartments (Ct.DMD, Tb.DMB), the quantitative grayscale volumes were multiplied by the segmented cortical and trabecular bone volumes.

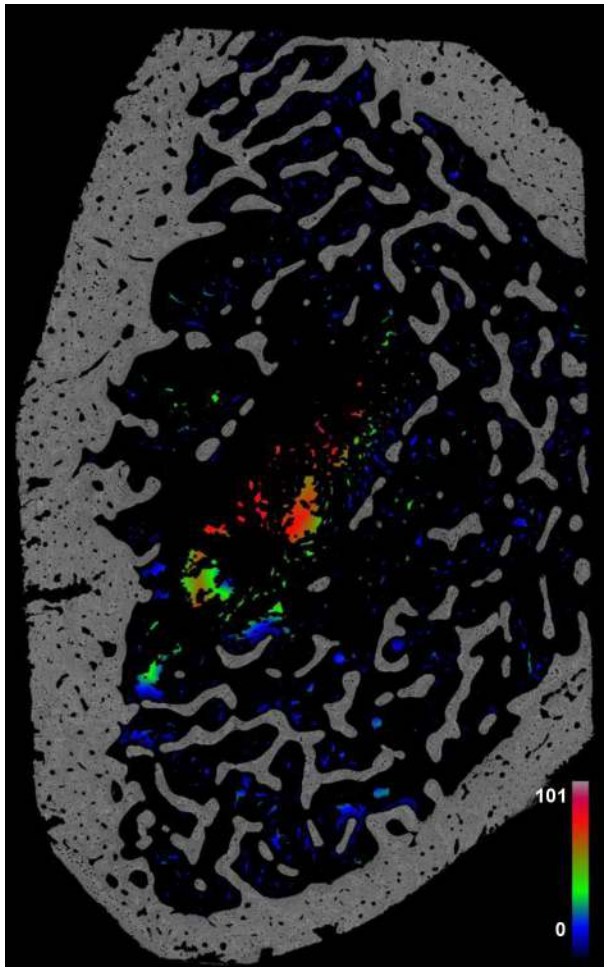

Fig. 7. Measurement of the vascular-trabecular interdistance (VTI). The 3D distance map from background to Tb is multiplied with Vi to yield the distance to Tb in each point in Vi. The figure shows a 2D slice of this distance map, color corresponding to distance in μm, superimposed over the bone volume, shown in grayscale.

E. Vascular-Trabecular Interdistance (VTI)

Since we have access to both bone and vessel microstructures simultaneously, it seemed interesting to define a measure that relates the two quantitatively. Therefore, we propose a new parameter relating to both bone and vessels. It is defined as the average of the local distance from each point in the Vi compartment to the Tb compartment, and we designate it the vascular-trabecular interdistance (VTI).

Let $\mathbf{Z}^3$ be a three-dimensional discrete space, and X an object in $\mathbf{Z}^3$. Let $d(x, x')$ be a discrete distance between two points in $\mathbf{Z}^3$. We use here the (3,4,5) Chamfer distance [20] which has been shown to be a good approximation of the Euclidean distance [21]. The distance transform DT, defined from $\mathbf{Z}^3$ to $\Re^+$, associates to each voxel its distance to the complement of X (denoted $\neg X$):

$$\mathrm{DT}(x) = d(x, \neg X) = \inf \{d(x, y) \,|\, y \in \neg x\} \,. \qquad (1)$$

TABLE I
MEDIANS AND INTERQUARTILE RANGES FOR THE MEASURED PARAMETERS. ASTERISK $(*)$ INDICATES SIGNIFICANT DIFFERENCE $(\mathrm{p} < 0.05)$

	ROI1			ROI2		
	CTRL		PTH	CTRL		PTH
ViV/IV (%)	3.38 (1.40)		3.11 (1.75)	3.76 (2.96)	*	2.51 (1.38)
ViV/Ma.V (%)	4.47 (2.09)		5.60 (2.81)	3.81 (3.27)		2.56 (1.31)
VcV/Ct.TV (%)	0.95 (0.17)		1.37 (0.60)	0.19 (0.08)		0.14 (0.01)
Vi.Th (μm)	53.0 (13.6)		63.4 (24.9)	73.9 (12.5)	*	94.9 (20.6)
Vc.Th (μm)	22.6 (2.64)		25.0 (6.81)	18.3 (2.27)		19.03 (1.63)
BV/TV (%)	36.3 (3.92)		49.4 (7.83)	49.0 (4.82)		55.2 (3.40)
Ct.BV/TV (%)	15.9 (7.13)		18.2 (9.60)	48.5 (3.65)	*	52.1 (4.81)
Ct.TV/TV (%)	18.6 (7.56)		23.2 (11.2)	51.8 (3.74)	*	54.8 (4.62)
Tb.V/IV (%)	22.4 (2.07)	*	38.9 (5.43)	3.89 (4.15)		3.32 (5.20)
Tb.TV/IV (%)	23.4 (2.33)	*	41.6 (5.57)	4.01 (4.32)		3.41 (5.33)
Ma.V/TV (%)	60.8 (4.49)	*	43.8 (8.81)	48.3 (4.57)	*	41.8 (3.66)
Tb.Po (%)	4.37 (0.66)		6.02 (0.73)	3.40 (0.88)		3.64 (0.76)
Ct.Po (%)	13.7 (2.64)		17.6 (6.28)	5.03 (1.42)		4.69 (0.63)
Ct.Th (mm)	0.762 (0.128)		0.863 (0.149)	1.16 (0.098)	*	1.25 (0.057)
Tb.Th (mm)	0.176 (0.004)	*	0.220 (0.007)	0.135 (0.063)		0.133 (0.073)
Ct.DMB (g/cm^3)	0.808 (0.009)	*	0.788 (0.030)	0.828 (0.050)		0.822 (0.005)
Tb.DMB (g/cm^3)	0.776 (0.026)		0.730 (0.019)	0.749 (0.036)	*	0.748 (0.063)
VTI (μm)	25.1 (7.20)	*	16.5 (7.77)	70.3 (23.1)	*	83.0 (33.5)

Assuming that the relevant compartments, trabecular bone (Tb) and internal vessels (Vi), have been segmented from the data, so that Tb and Vi are binary volumes, the first step in calculating VTI is to calculate the distance transform from background to trabecular bone, $\mathrm{DT}(\neg\mathrm{Tb})$. This is then multiplied pointwise with Vi to yield the distance map from each point in Vi to Tb, that is $d(x)$. A 2D slice through this distance map is shown in Fig. 6. VTI can then be defined as the average distance from Vi to Tb as

$$\mathrm{VTI} = \sum_{x \in \mathrm{Vi}} \frac{d(x, Tb)}{|\mathrm{Vi}|}, \tag{2}$$

where $|\cdot|$ denotes cardinality.

To verify changes in the VTI, a histologic study was performed. The osteoid-vascular distance was measured in the metaphysis of the proximal tibia using histomorphometry and analysis of Goldner Trichrome slides. Samples from 8 rats were analysed (4 controls, 4 from the PTH group). Five slides/rat were examined.

F. Statistical Analysis

Statistical testing was performed between the two groups on all measured parameters, in each ROI separately. Several parameters could not be considered normally distributed (Lilliefors test, $\mathrm{p} < 0.05$), hence, the Mann-Whitney U-test was used in all cases. Differences between the two groups were considered statistically significant at the 5% level $(\mathrm{p} < 0.05)$. Data points lying 3 interquartile ranges outside the quantiles were identified as potential outliers and removed if appropriate (reasons for removal where leakage of contrast agent, unsuccessful perfusion and images discovered to be taken in the wrong anatomical position). In total, 28 samples were included in the statistical analysis, 13 controls and 15 from the PTH group.

III. RESULTS

Several significant differences between the two groups were detected. These are summarized in Table I.

Bone volume: PTH treated rats had 30% higher cortical bone ratio ($\mathrm{p} = 0.03$ with respect to the cortical envelope volume, $\mathrm{p} = 0.039$ with respect to the cortical volume), 40% higher in ROI1 $(\mathrm{p} < 0.0001)$ and 10% higher in ROI2 $(\mathrm{p} = 0.0364)$. PTH treated rats had 70% greater trabecular volume ratio $(\mathrm{p} < 0.0001)$ and trabecular envelope ratio $(\mathrm{p} < 0.0001)$, both in ROI1. PTH treated rats also had a slightly higher cortical envelope ratio in ROI2 $(\mathrm{p} = 0.0455)$.

Bone thickness: Rats treated with PTH showed a 50% increase in cortical thickness $(\mathrm{p} < 0.0001)$ and 30% increase in trabecular thickness in ROI1 $(\mathrm{p} < 0.0001)$.

Bone mineralization: the control group showed 10% higher average mineralization in ROI1 $(\mathrm{p} = 0.0003)$.

Marrow volume: PTH treated rats showed a 20% decrease of marrow volume ratio $(\mathrm{p} < 0.0001)$

Total Vessel Volume: PTH treated rats showed a decrease in vessel volume by 27% $(\mathrm{p} = 0.0451)$.

Vessel thickness: PTH treated rats showed an increase in thickness of the internal vessels by 30% $(\mathrm{p} = 0.0040)$.

Vascular-trabecular interdistance: Rats treated with PTH showed a 24% decrease in VTI $(\mathrm{p} < 0.0001)$. Histograms of one PTH sample and one control is shown in Fig. 8. Note the shift towards smaller distances in the PTH sample. The osteoid-vascular distance was found to be significantly lower in the PTH group (Fig. 9).

IV. DISCUSSION AND CONCLUSION

SR-μCT allowed for the first time to study simultaneously bone microstructure and microvascularization at very high spatial resolution. Due to adapted image analysis, it was possible

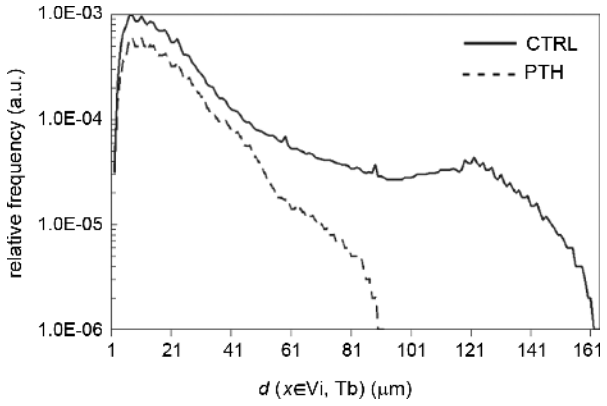

Fig. 8. Histograms of $d(x \in \mathrm{Vi},\ \mathrm{Tb})$ for a sample treated with PTH and a control sample.

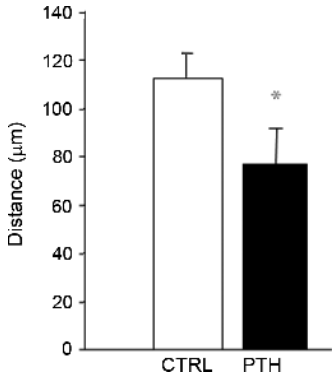

Fig. 9. Osteoid-vascular distance measured by histomorphometry and Goldner-Trichrome slides. The asterisk denotes significance at the 5% level.

to extract from the data a large number of 3D quantitative parameters. A new parameter was also defined, the vascular-trabecular interdistance (VTI) which relates the bone and vascular microstructures. This parameter can be viewed as quantifying the spatial organization of the microvascularization relative to the trabecular structure.

The method was applied to study the effect of PTH treatment on bone microvascularization. The results demonstrated that PTH modulated both bone and vascular parameters (e.g., BV/TV, Tb.V, Ct.V, V.Th, etc.). The increases in bone volume and trabecular and cortical thicknesses are in agreement with previous studies.

Experimental studies have demonstrated augmented bone mass with intermittent PTH administration in mice, rats and humans. For example, mice treated intermittently $(40\ \mu\mathrm{g/kg/d})$ for 3 and 7 wks had increases in trabecular area, trabecular number, and trabecular and cortical widths of the proximal tibia [22]. In addition, regardless of age, PTH administered for 1 wk in 1-, 3-, and 13-month-old female Sprague-Dawley rats augmented bone formation rate and bone volume-to-total volume ratio [23]. As demonstrated in many clinical trials, the therapeutic effects of intermittent PTH administration are evident in humans as well. Following 21 months of daily treatment, the occurrence of vertebral fractures in post-menopausal women was reduced to 5% and 4% in groups receiving 20 μg and 40 μg of PTH, respectively, in comparison to the 14% occurrence rate observed in patients in the placebo group [24]. In addition to determining the change in bone volume with PTH administration, the current study examines the effects on the bone vasculature. 3D vessel thicknesses were significantly increased with PTH treatment.

SR μCT also permitted the analysis of the degree of bone mineralization in 3D, which was diminished with intermittent PTH administration. The VTI was also strongly modulated due to PTH treatment. The decrease in VTI can be interpreted as vessels growing closer to the trabecular wall. This could imply an increased oxygen transport to the bone

We acknowledge that although the volume of data was very large (about 100 GB), the number of samples analyzed is limited at present. Further data has been acquired and will be analyzed with the present methods to augment the number of samples and make the statistical analysis more robust. Further work will also include adaptation of the method to mouse bone, which sets different requirements on the whole chain, from contrast agent to imaging setup and data analysis.

REFERENCES

[1] B. Arora, R. Mesa, and A. Tefferi, "Angiogenesis and anti-angiogenic therapy in myelofibrosis with myeloid metaplasia," *Leuk. Lymphoma*, vol. 45, pp. 2373–2386, 2004.

[2] J. F. Griffith, D. K. Yeung, P. H. Tsang, K. C. Choi, T. C. Kwok, A. T. Ahuja, K. S. Leung, and P. C. Leung, "Compromized bone marrow perfusion in osteoporosis," *J. Bone Miner. Res.*, vol. 23, pp. 1068–1075, 2008.

[3] F. H. Sim and P. J. Kelly, "Relationship of bone remodeling, oxygen consumption, and blood flow in bone," *J. Bone Joint Surg. Am.*, vol. 52, pp. 1377–1389, 1970.

[4] Z. Yao, M. H. Lafage-Proust, J. Plouët, S. Bloomfield, C. Alexandre, and L. Vico, "Increase of both angiogenesis and bone mass in response to exercise depends on VEGF," *J. Bone Miner. Res.*, vol. 19, pp. 1471–1480, 2004.

[5] R. Müller, "Hierarchical microimaging of bone structure and function," *Nat. Rev. Rheumatol.*, vol. 5, pp. 375–381, 2009.

[6] R. Voide, P. Schneider, M. Stauber, P. Wyss, M. Stampanoni, U. Sennhauser, G. H. van Lenthe, and R. Müller, "Time-lapsed assessment of microcrack initiation and propagation in murine cortical bone at submicrometer resolution," *Bone*, vol. 45, pp. 164–173, 2009.

[7] H. Follet, F. Peyrin, E. Vidal-Salle, A. Bonnassie, C. Rumelhart, and P. J. Meunier, "Intrinsic mechanical properties of trabecular calcaneus determined by finite-element models using 3D synchrotron microtomography," *J. Biomech.*, vol. 40, pp. 2174–2183, 2007.

[8] C. Chappard, A. Basillais, L. Benhamou, A. Bonassie, B. Brunet-Imbault, N. Bonnet, and F. Peyrin, "Comparison of synchrotron radiation and conventional x-ray microcomputed tomography for assessing trabecular bone microarchitecture of human femoral heads," *Med. Phys.*, vol. 33, pp. 3568–3577, 2006.

[9] S. Bayat, L. Apostol, E. Boller, T. Brochard, and F. Peyrin, "In vivo imaging of bone micro-architecture in mice with 3D synchrotron radiation micro-tomography," *Nucl. Instrum. Methods Phys. Res. A*, vol. A548, pp. 247–252, 2005.

[10] J. S. Thomsen, A. Laib, B. Koller, S. Prohaska, L. Mosekilde, and W. Gowin, "Stereological measures of trabecular bone structure: Comparison of 3D micro computed tomography with 2D histological sections in human proximal tibial bone biopsies," *J. Microsc.*, vol. 218, pp. 171–179, 2005.

[11] V. Bousson, F. Peyrin, C. Bergot, M. Hausard, A. Sautet, and J. D. Laredo, "Cortical bone in the human femoral neck: Three-dimensional appearance and porosity using synchrotron radiation," *J. Bone Miner. Res.*, vol. 19, pp. 794–801, 2004.

[12] M. Salomé, F. Peyrin, P. Cloetens, C. Odet, A.-M. Laval-Jeantet, J. Baruchel, and P. Spanne, "A synchrotron radiation microtomography system for the analysis of trabecular bone samples," *Med. Phys.*, vol. 26, pp. 2194–2204, 1999.

[13] S. Nuzzo, F. Peyrin, P. Cloetens, J. Baruchel, and G. Boivin, "Quantification of the degree of mineralization of bone in three dimensions using synchrotron radiation microtomography," *Med. Phys.*, vol. 29, pp. 2672–2681, 2002.

[14] D. C. Moore, C. W. Leblanc, R. Muller, J. J. Crisco, III, and M. G. Ehrlich, "Physiologic weight-bearing increases new vessel formation during distraction osteogenesis: A micro-tomographic imaging study," *J. Orthop. Res.*, vol. 21, pp. 489–496, 2003.

[15] X. Zhang, C. Xie, A. S. Lin, H. Ito, H. Awad, J. R. Lieberman, P. T. Rubery, E. M. Schwarz, R. J. O'Keefe, and R. E. Guldberg, "Periosteal progenitor cell fate in segmental cortical bone graft transplantations: Implications for functional tissue engineering," *J. Bone Miner. Res.*, vol. 20, pp. 2124–2137, 2003.

[16] J.-C. Labiche, O. Maton, S. Pascarelli, M. A. Newton, G. C. Ferre, C. Curfs, G. Vaughan, A. Homs, and D. F. Carreiras, "The FReLoN camera as a versatile X-ray detector for time resolved dispersive EXAFS and diffraction studies of dynamic problems in materials science, chemistry, and catalysis," *Rev. Sci. Instrum.*, vol. 78, p. 091301, 2007.

[17] N. Otsu, "A threshold selection method from gray level histograms," *IEEE Trans. Syst. Man Cybern.*, vol. 9, pp. 62–66, 1979.

[18] T. Hildebrand and P. Rüegsegger, "A new method for the model-independent assessment of thickness in three-dimensional images," *J. Microsc.*, vol. 185, pp. 67–75, 1997.

[19] E. Martín-Badosa, A. Elmoutaouakkil, S. Nuzzo, D. Amblard, L. Vico, and F. Peyrin, "A method for the automatic characterization of bone architecture in 3D mice microtomographic images," *Comput. Med. Imaging Graph.*, vol. 27, pp. 447–458, 2003.

[20] U. Montanari, "Continuous skeletons from digitized images," *J. Assoc. Comput. Mach.*, vol. 16, pp. 534–549, 1969.

[21] G. Borgefors, "Distance transformations in Arbitrary dimensions," *Comput. Vis. Graph. Imag. Proc.*, vol. 27, pp. 321–345, 1984.

[22] A. Iida-Klein, H. Zhou, S. S. Lu, L. R. Levine, M. Ducayen-Knowles, D. W. Dempster, J. Nieves, and R. Lindsay, "Anabolic action of parathyroid hormone is skeletal site specific at the tissue and cellular levels in mice," *J. Bone Miner. Res.*, vol. 17, pp. 808–816, 2002.

[23] G. Friedl, R. T. Turner, G. L. Evans, and H. Dobing, "Intermittent parathyroid hormone (PTH) treatment and age-dependent effects on rat cancellous bone and mineral metabolism," *J. Orthop. Res.*, vol. 25, pp. 1454–1464, 2007.

[24] R. M. Neer, C. D. Arnaud, J. R. Zanchetta, R. Prince, G. A. Gaich, J. Y. Reginster, A. B. Hodsman, E. F. Eriksen, S. Ish-Shalom, H. K. Genant, O. Wang, and B. H. Mitlak, "Effect of parathyroid hormone (1–34) on fractures and bone mineral density in postmenopausal women with osteoporosis," *New Engl. J. Med.*, vol. 344, pp. 1434–1441, 2001.